JACS
JOURNAL OF THE AMERICAN CHEMICAL SOCIETY
pubs.acs.org/JACS
Article

Mixed Cationic and Anionic Redox in Ni and Co Free Chalcogen-Based Cathode Chemistry for Li-Ion Batteries

Sudhan Nagarajan, Sooyeon Hwang, Mahalingam Balasubramanian, Naresh Kumar Thangavel, and Leela Mohana Reddy Arava*

Cite This: J. Am. Chem. Soc. 2021, 143, 15732−15744
Read Online
ACCESS | Metrics & More | Article Recommendations | Supporting Information

ABSTRACT: Mixed cationic and anionic redox cathode chemistry is emerging as the conventional cationic redox centers of transition-metal-based layered oxides are reaching their theoretical capacity limit. However, these anionic redox reactions in transition metal oxide-based cathodes attained by taking excess lithium ions have resulted in stability issues due to weak metal−oxygen ligand covalency. Here, we present an alternative approach of improving metal−ligand covalency by introducing a less electronegative chalcogen ligand (sulfur) in the cathode structural framework where the metal d band penetrates into the ligand p band, thereby utilizing reversible mixed anionic and cationic redox chemistry. Through this design strategy, we report the possibility of developing a new family of layered cathode materials when partially filled d orbital redox couples like $Fe^{2+/3+}$ are introduced in the Li-ion conducting phase (Li_2SnS_3). Further, the electron energy loss spectroscopy and X-ray absorption near-edge structure analyses are used to qualitatively identify the charge contributors at the metal and ligand sites during Li^+ extraction. The detailed high-resolution transmission electron microscopy and high annular dark field-scanning transmission electron microscopy investigations reveal the multi-redox induced structural modifications and its surface amorphization with nanopore formation during cycling. Findings from this study will shed light on designing Ni and Co free chalcogen cathodes and various functional materials in the chalcogen-based dual anionic and cationic redox cathode avenue.

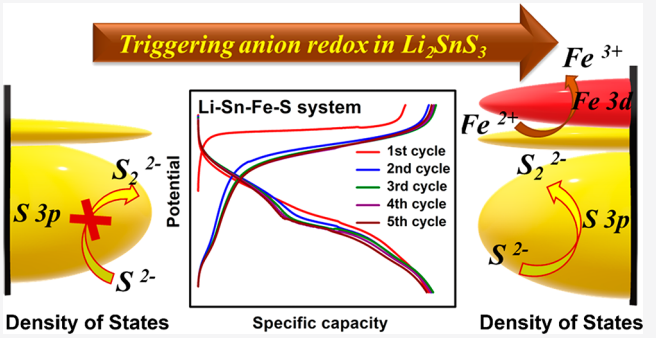

INTRODUCTION

The first commercial Li-ion battery (LIB) was released in 1991, which comprised a $LiCoO_2$ cathode, graphite anode, and lithium-ion-containing electrolyte.[1,2] Even after 30 years of active research, the current Li-ion battery technology has reached a plateau and needs to be improved in terms of energy density and cyclability to meet growing energy needs. In general, the conventional cathodes such as $LiCoO_2$ (LCO), $LiFePO_4$ (LFP), $LiNiMnCoO_2$ (NMC), and $LiNiCoAlO_2$ (NCA) are based on the redox chemistries of transition metals, and their capacity utilization is compensated solely by transition metal ions (cationic redox offering specific capacity in the range of 150−200 mAh/g).[2] Further, the researchers have been trying to extend the capacity as well as energy density toward 250 mAh/g and 500 Wh/kg, respectively.[3] With this motivation, in recent years, researchers have been exploring the so-called "Li-rich anion redox" cathode chemistry, wherein electrons stored on oxide anions are reversibly utilized during redox reaction along with transition metal redox.[4] The combined redox of both anion and cation causes significantly higher energy storage capability from these Li-rich cathode materials.

In Li-rich anion redox cathodes, rigorous research was carried out by many research groups to understand their structural and electrochemical properties and eventually commercialize them for next-generation LIBs. Among various cathode materials, the layered cathodes such as $Li_{1.2}Ni_{0.15}Mn_{0.55}Co_{0.1}O_2$ and $Li_{1.2}Ni_{0.2}Mn_{0.6}O_2$ and disordered rock salt cathodes such as $Li_{1.3}Ni_{0.27}Nb_{0.43}O_2$ and $Li_{1.3}Mn_{0.4}Nb_{0.6}O_2$ are popular as they deliver a high capacity of 250 mAh/g at room temperature.[5,6] The attractive anion redox chemistry was well investigated by Tarascon and his co-workers in model anion redox cathodes and Li-rich NMC by various research groups around the world.[7−13] Even after rigorous research in the field of anion redox chemistry, the lithium-rich cathodes have not been commercialized yet due to their unsolved fundamental issues of voltage fade, voltage hysteresis, and irreversible oxygen release.[14] Though several

Received: July 1, 2021
Published: September 15, 2021

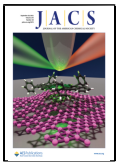

mitigation strategies have been introduced while understanding the redox mechanism through advanced characterization tools including X-ray absorption spectroscopy,[15] hard X-ray photoelectron spectroscopy,[10,16] resonant inelastic X-ray scattering,[13,17,18] and nuclear magnetic resonance[19,20] and Raman spectroscopy,[21,22] gaining fundamental knowledge is being evolved continuously as the rationalized understanding of its failure mechanism is not yet clear.

The anion redox phenomenon was well investigated in practical Li-rich NMC material and Ru-, Ir-based model compounds, and it was proven that the oxygen redox stabilization is intrinsically improved by raising transition metal and oxygen ligand covalency as the Ru exhibited higher oxygen redox stabilization than Mn.[7,23,24] The driving force for improved anion redox reaction is metal−ligand covalency, and the property could be improved to achieve efficient anion redox stabilization in contrast to unstable oxygen anion redox in oxide cathodes. To improve the metal−ligand covalency, the strategy of replacing the oxide ligand with the chalcogen (S, Se) ligand is emerging, where the less electronegative nature of the chalcogen improves the ligand p band penetration into the metal d band with a combination of appropriate metals and chalcogen ligands. Back in the 1990s, the replacement of less electronegative chalcogens in transition metal chalcogenide compounds and their anion cation redox competition behavior were well investigated by Rouxel et al.[25−27] With this promising chalcogen chemistry, Tarascon and his co-workers revisited one of the early layered chalcogen structures and identified its electrochemical performance and possibility of utilizing this chemistry for next-generation cathodes.[28] The results exhibited superior performance in terms of voltage fade, voltage hysteresis, and capacity fade. This work indicates a proof of concept that the chalcogen anion redox in a Li-rich cathode is possible, and it calls for materials researchers to further design unexplored chalcogen anion redox compounds elucidating the structure−property relationship. Even though few research reports have revisited chalcogen cathodes, both Li-rich and conventional chalcogen cathodes, the evolution of chalcogen anion redox cathode chemistry is at its infancy.[29−31] On the basis of their thermodynamic stability and synthesizability, design rules for developing available chalcogen anion redox cathode compounds need to be investigated which could potentially lead to achieving unexplored cathode materials and taking advantage of their attractive properties.

With this motivation, the search of new cathode material design in chalcogen materials was attempted and proved that chalcogen-based Li-ion conducting phases could be utilized for electrode materials design of mixed anionic and cationic redox cathodes with partially filled d orbital redox couple substitution. To prove this concept, here we introduce mixed anionic and cationic redox activity in Li_2SnS_3, which is one of the fast Li-ion conductors, by substituting the Fe redox couple in the host cation Sn site that triggered the sulfur anionic redox and led to Ni and Co free chalcogen-based mixed anionic and cationic redox Li-ion cathode materials. This research focuses on electronic structure, electrochemical behavior, and lithiation-delithiation induced structural degradation of the Fe redox couple substituted Li_2SnS_3 cathodes through advanced spectroscopy and high-resolution microscopy investigations.

RESULTS AND DISCUSSION

Structural Evaluation. The targeted materials with various quantities of Fe^{2+} substitutions were carried out using conventional solid-state synthesis. The pristine material Li_2SnS_3 appeared to be dark green crystals, and the color changed to uniform brown-colored crystals after Fe substitution, which implies that the substitution occurred homogeneously (Figure S1). In addition, the homogeneous presence of iron after substitution is shown in Figure S2. The Li_2SnS_3 was synthesized, and its structure−property relationship was previously reported in the literature by Brant et al. in 2015.[32] This Li-ion conducting compound (Li_2SnS_3) was identified as a sodium chloride like structure type where each Sn^{4+} and Li^+ ion is octahedrally coordinated with S atoms. The Sn^{4+} ions reside on the metal layer, and the Li ions reside on the Li layer as well as the Sn metal layer in the layered structural framework. The substitution of Fe^{2+} was carried out in the $Li_{1.33}Sn_{0.67}S_2$ (Li_2SnS_3) phase, and different Fe^{2+} levels starting from 0.1 to 0.4 were synthesized according to this design formula $Li_{1.33-2y/3}M_{0.67-y/3}Fe_yS_2$ (M = tetravalent metal ion, $0 \le y \le 0.4$). Recently, the similar design formula was successfully used to prepare a Li-rich chalcogen anion redox compound by Tarascon and his co-workers, and the authors demonstrated anion redox performance in Ti-based Li-rich chalcogen cathodes for the first time.[28] Other than Ni and Co redox couples, Ti and Fe redox couples are common in battery materials especially $Li_4Ti_5O_{12}$ and $LiFePO_4$.[33,34] The Ti is commonly in the tetravalent state (Ti^{4+}), which is a fully emptied d orbital configuration ($3d^0$), implying that the Ti will not be oxidized further in the potential region of interest in this study. Stabilizing Ti in a lower oxidation state needs synthesis optimization that leads to additional challenges. With these challenges, an alternative and cheap redox couple is the Fe redox couple whose redox reactions are well investigated in sulfide frameworks for Li-ion battery cathode materials.[35] In addition, triggering anionic redox in a chalcogen framework needs a redox couple that is pinned on top of the chalcogen anion *p* band, thereby covalent mixing of the redox couple d band and chalcogen anion *p* band will lead to reversible cationic and anionic redox reactions during Li extraction.[36] With this fundamental necessity, the Fe redox is preferred as a model redox couple to activate the anion redox phenomenon in the $Li_{1.33}Sn_{0.67}S_2$-based chalcogen framework for the first time, and further, this research can be explored to develop Ni and Co free mixed anionic and cationic redox cathode chemistry for Li-ion battery applications. The X-ray powder diffraction patterns of simulated $Li_{1.33}Sn_{0.67}S_2$, pristine $Li_{1.33}Sn_{0.67}S_2$, and various Fe substituted compounds prepared in this work are shown in Figure S3. From the diffraction pattern, the simulated $Li_{1.33}Sn_{0.67}S_2$ powder pattern[32] matches with the pristine $Li_{1.33}Sn_{0.67}S_2$ powder pattern which confirms the $Li_{1.33}Sn_{0.67}S_2$ phase formation. Hereafter, the Fe substituted compounds are named as X Fe-$Li_{1.33}Sn_{0.67}S_2$ (X: amount of Fe^{2+} substitution). Further, the $Li_{1.33}Sn_{0.67}S_2$ Li-ion conducting phase was substituted with the Fe redox couple and the powder patterns were not changed significantly up to 0.3 Fe substitution, implying that the substitution mixed well with the $Li_{1.33}Sn_{0.67}S_2$ framework over a compositional range up to 0.3 Fe substitution. However, the substitution beyond 0.3 Fe is not matching with the simulated, pristine, and other Fe substituted compositions which confirms the Fe substitution threshold in this layered structural framework. Also, the additional peak

https://doi.org/10.1021/jacs.1c06828
J. Am. Chem. Soc. 2021, 143, 15732−15744

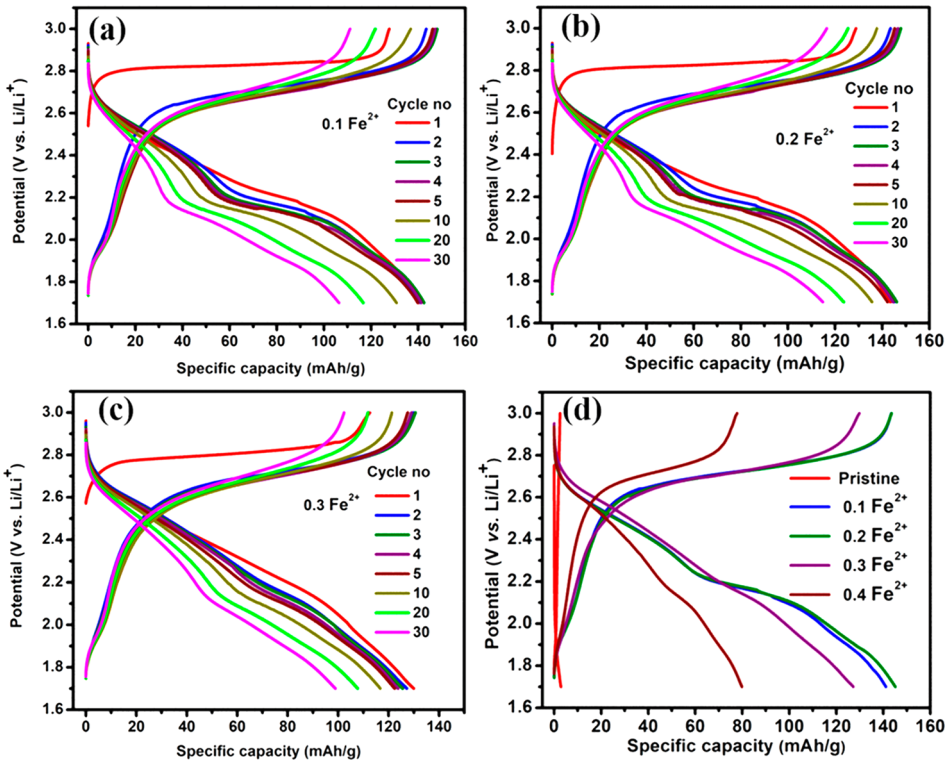

Figure 1. Electrochemical performance of Sn-based chalcogen anion redox cathodes. Galvanostatic charge-discharge profiles of (a) 0.1Fe-$Li_{1.33}Sn_{0.67}S_2$, (b) 0.2Fe-$Li_{1.33}Sn_{0.67}S_2$, and (c) 0.3Fe-$Li_{1.33}Sn_{0.67}S_2$ at 10 mA/g current density. (d) Charge-discharge profile comparison of different Fe substitutions at 10 mA/g current density.

emerged around ∼26° which may be attributed to the impurity peak of Li_2S from the precursor. Further, the pristine and Fe substituted compositions were electrochemically analyzed for identifying Li^+ storage properties.

Electrochemical Investigation. The electrochemical lithiation (discharge)-delithiation (charge) behavior was investigated in Fe redox couple substituted Sn-based chalcogen cathodes (0.1−0.4 Fe in $Li_{1.33}Sn_{0.67}S_2$ host). All the electrode compositions were cycled in conventional 1 M $LiPF_6$ in EC:DMC electrolyte combination without any additives. The galvanostatic charge-discharge profiles of these compounds are shown in Figure 1 and Figure S4. The voltage profiles of the pristine composition exhibited negligible lithiation-delithiation behavior, indicating that the composition ($Li_{1.33}Sn_{0.67}S_2$) is inactive in the potential region (1.7−3 V vs Li/Li^+) due to the high oxidation state of the Sn cation in which the Sn^{4+} is fully occupied with $4d^{10}$ orbital configurations. Therefore, the pristine composition exhibited negligible lithiation and delithiation behavior in the potential region (1.7−3 V vs Li/Li^+) used in this study. This behavior is evidenced with the charge-discharge profiles of the pristine composition and shown in the Supporting Information (Figure S4). Though the pristine composition has a rich nature of sulfide ligand, the sulfide anion redox was not activated as the stable Sn^{4+} d states are not pinned to the sulfur 3p ligand band. Hence, it is hypothesized that introducing a partially filled d orbital transition metal into the pristine $Li_{1.33}Sn_{0.67}S_2$ composition would allow accessing anionic redox along with cationic redox activity. As per Figure 1a−c, the Fe redox couple substituted compositions exhibited reversible Li insertion-extraction properties with sloppy voltage profiles. In all Fe substituted compositions, the charge-discharge curves showed dissimilarity; especially the first charge curve has plateau-like behavior (∼2.8 V vs Li/Li^+), in contrast to consequent charge-discharge profiles. Besides, the first charge cycle exhibited less capacity (less Li extraction) than the first discharge capacity that may be attributed to the Li deficient nature during the pristine state. Therefore, during the first charge, the capacity is less due to the less extraction of Li from the structure, but the maximum Li occupation in the structure was electrochemically achieved during discharge which is why the first discharge capacity is higher than the charge capacity. A similar phenomenon was observed in various Li-based layered chalcogenides and discussed by Goodenough and co-workers.[36] The dissimilarity in charge−discharge profile also proves that the structural path during the first charge (delithiation) is completely different from the discharge (lithiation) structural path as the similar behavior was observed in previous chalcogen-based research reports.[29,30] Further, the consequent cycles showed plateau-like charge behavior at slightly higher potential and sloppy discharge profiles with an inflection point around ∼2.2 V vs Li/Li^+, indicating that the lithiation and delithiation structural path is different during charge and discharge. The different lithiation and delithiation structural path mechanisms were already evidenced in various Li-ion cathodes.[37] The observed voltage profiles are comparatively different than what is observed in the seminal Li-rich NMC composition and Li-rich chalcogen cathodes.[28] Moreover, the inflection point around (∼2.2 V vs Li/Li^+) may be attributed to the lithiation-induced phase transformation as it exhibited significant lithiation path changes in the voltage profile. All the Fe substituted compositions were investigated, and the voltage profiles for continuous charge-discharge cycles are shown in the Figure 1a−c and Figure S4. In comparison to various Fe

https://doi.org/10.1021/jacs.1c06828
J. Am. Chem. Soc. 2021, 143, 15732−15744

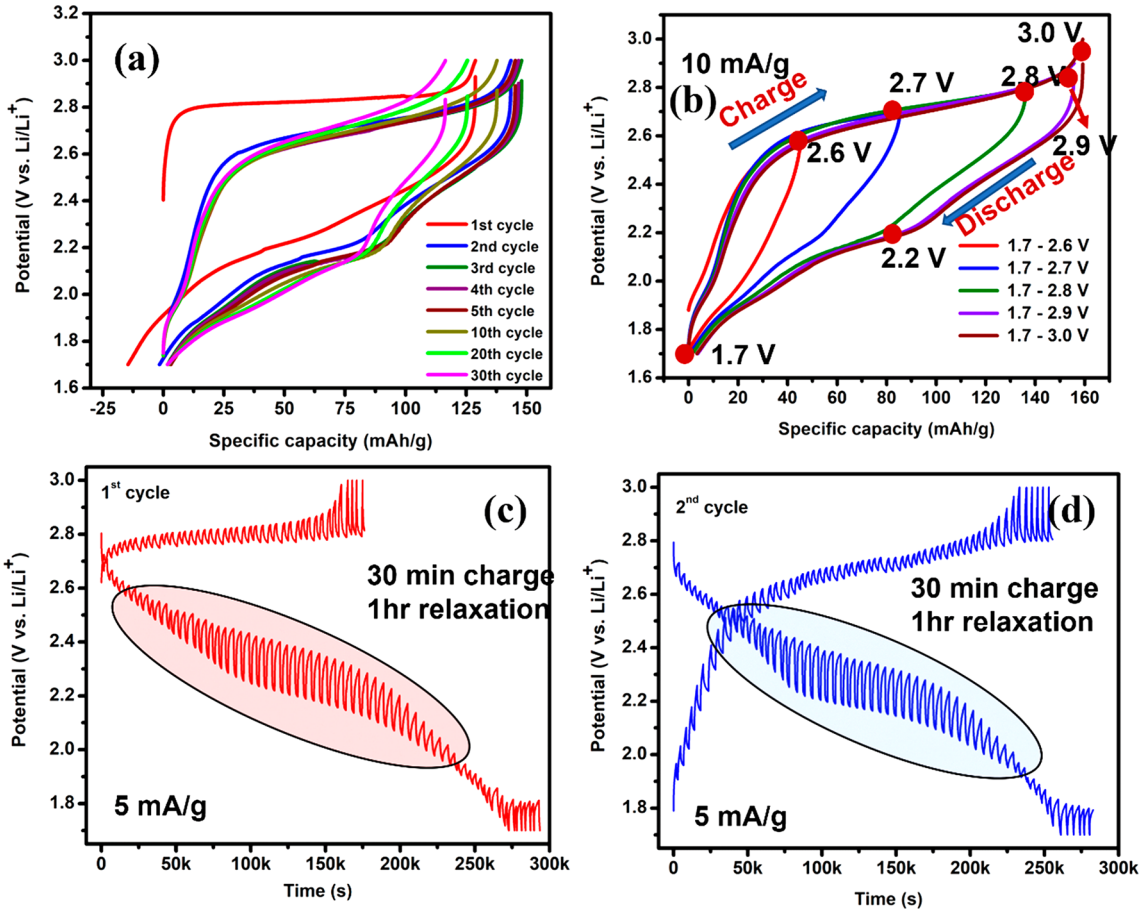

Figure 2. Electrochemical kinetic study of the Sn-based chalcogen anion redox cathode (0.2Fe-$Li_{1.33}Sn_{0.67}S_2$). (a) Voltage hysteresis profile of active cathode material at 10 mA/g current density. (b) Voltage profile of the cathode at different upper cut-off potentials. GITT profiles of active cathode material: (c) 1st cycle and (d) 2nd cycle GITT profiles with 30 min pulse and 1 h relaxation.

substituted compositional ranges, the composition with 0.2 Fe substitution in $Li_{1.33}Sn_{0.67}S_2$ (pristine) system exhibited superior performance over other compositions (Figure 1d), and the composition was further investigated for understanding its possible charge compensation mechanisms. Fundamentally, substitution of partially filled Fe^{2+} d states in the conduction band will affect the Fermi level and S 3p character which leads to a significant change in voltage profiles and capacity after different Fe^{2+} substitutions, and this observation is consistent with the seminal Li-rich chalcogen cathode work by Saha et al.[28] Despite exhibiting reversible capacity, the voltage profiles in almost all the compositions nested to large voltage hysteresis, and the origin of the capacity fade and voltage hysteresis will be associated with any possible structural transformation and Li-ion kinetic limitations during electrochemical reactions, respectively.

Electrochemical Kinetic Study. From the voltage profiles, it is clearly seen that the charge-discharge profiles exhibited huge hysteresis (0.511 V at 50% state of charge) starting from the first cycle; a voltage hysteresis plot for the 1st cycle to the 30th cycle is shown in Figure 2a. To understand the hysteresis further, we attempted to analyze the effect of the upper cut-off potential on the voltage hysteresis (Figure 2b). Unfortunately, the results had no significant effect on the voltage hysteresis, which implies that the hysteresis in the Sn-based chalcogen system may be originated from the intrinsic nature of the Li insertion extraction reactions in this 0.2 Fe substituted combination. With this observation, to further analyze the process of Li insertion extraction from the cathode, the galvanostatic intermittent titration technique (GITT) measurement was carried out in the current density of 5 mA/g for an interval of 30 min, followed by an open circuit state for 1 h, to allow the cell voltage to relax to a steady state. The GITT measurement is a quasi-steady state chronopotentiometry measurement and reliable to evaluate the chemical diffusion coefficient of the Li insertion extraction reactions.[38] The GITT measurements on the composite electrodes for complete two continuous cycles are shown in Figure 2c,d. The overpotential term is used in this measurement which is the difference between the potential with a current pulse and the potential during the relaxed state at each interval. The first charge process exhibited less overpotential with a gradual increment, and the discharge process delivered a huge overpotential with complete sloppy behavior like typical charge-discharge voltage profiles. The less overpotential with gradual increment is due to the smooth and kinetically faster Li extraction (charge) process from the 0.2 Fe substituted composite cathode compared to the Li insertion (discharge) process. The Li insertion is kinetically much slower and limited compared to the extraction (charge) process which was evidenced by the huge overpotential observed around 2.5−2.1 V during the insertion (discharge) process. Similarly, the second cycle showed less overpotential during charge and high overpotential with a clear inflection point at 2.2 V during

https://doi.org/10.1021/jacs.1c06828
J. Am. Chem. Soc. 2021, 143, 15732−15744

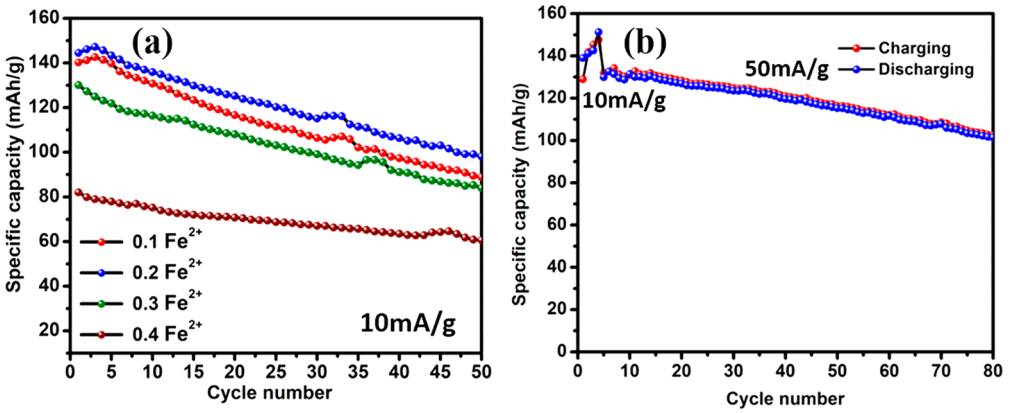

Figure 3. Electrochemical cycling stability of Sn-based chalcogen anion redox cathodes. (a) Cycling stability of different Fe substituted $Li_{1.33}Sn_{0.67}S_2$ compounds. (b) Cycling stability of 0.2Fe-$Li_{1.33}Sn_{0.67}S_2$ cathode at a high current density of 50 mA/g (initial few cycles at 10 mA/g).

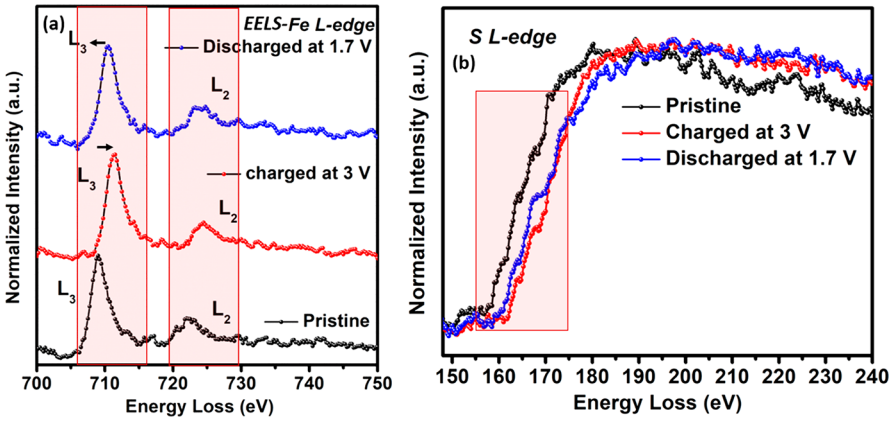

Figure 4. EELS measurements of 0.2Fe-$Li_{1.33}Sn_{0.67}S_2$ compound cycled at different states of charge: (a) Fe L edge and (b) S L edge measurements.

discharge. From the second cycle onward, the discharge profile regions were distinguished clearly with two different sloppy lithium insertion (charge) regions, indicating that this phenomenon may be due to the multiphase reaction regions and structural reconstruction. From the GITT profiles, the inflection point region displayed a high overpotential of ∼187 mV compared to other regions, indicating that the region is crucial where the electrochemical insertion of Li^+ ions is limited due to poor kinetics such as slow Li-ion diffusion and charge transfer resistance of Li insertion reactions.

To understand the extent of Li insertion and extraction, the cycling test for all the compounds was carried out in a half-cell configuration at the current density of 10 mA/g. Figure 3a exhibits superior electrochemical performance for 0.2 Fe substituted compounds compared to other compositions. In terms of capacity fade, there is a gradual deterioration in all the compounds cycled at a very low current density of 10 mA/g for 50 continuous cycles. Further, a cycling test of the 0.2 Fe substituted cathode was studied at 50 mA/g, exhibiting high rate cycling stability of 76% retention after 80 cycles (Figure 3b). The capacity degradation is mainly due to the multi-redox induced structural transformation, and this hypothesis was well evidenced with microscopy analysis in the later sections. Though the cycling stability of this compound is comparable to that of existing chalcogen anion redox cathodes,[28,29,39] we expect that nanostructuring and surface coatings strategies would enhance the cycle life further.[14,40,41] Further, the high loading of 10 mg/cm^2 cells exhibited excellent electrochemical performance at 10 mA/g current density, indicating that the Fe substituted composition exhibited good electronic and ionic conductivity in this chalcogen framework (Supporting Information, Figure S5).

Anion and Cation Redox Participation. To understand the redox processes in the chalcogen anion redox compound, various characterization tools have been used to qualitatively identify the redox participation of the elements present in the cathode compound. Among the compositional ranges, the 0.2 Fe substituted $Li_{1.33}Sn_{0.67}S_2$ exhibited superior electrochemical performance than other compositions. Therefore, this composition was used for analytical characterization throughout this work. To identify the cation redox in the cathode, initially, Fe L edge electron energy loss spectroscopy (EELS) measurement was carried out at different state of charge samples. The sample preparation for EELS measurements and procedures are given in the Supporting Information. Figure 4a shows the Fe $L_{2,3}$ edge spectrum for the pristine state, charged to 3 V, and discharged to 1.7 V samples. There are two peaks observed, and the first peak corresponds to the Fe L_3 peak, while the second peak corresponds to the Fe L_2 peak with an initial electronic state of p state. The L_3 peak is responsible for the Fe $2p_{3/2}$ initial state to Fe 3d final state transition, while the L_2 peak is for the Fe $2p_{1/2}$ to Fe 3d transition.[42] The large energy separation is due to the spin orbit interaction of the 2p core hole splitting the final state into two peaks in the range of 710−730 eV. Further, the Fe L edge energy was shifted to a high energy loss value when the cathode was charged to a full

https://doi.org/10.1021/jacs.1c06828
J. Am. Chem. Soc. 2021, 143, 15732−15744

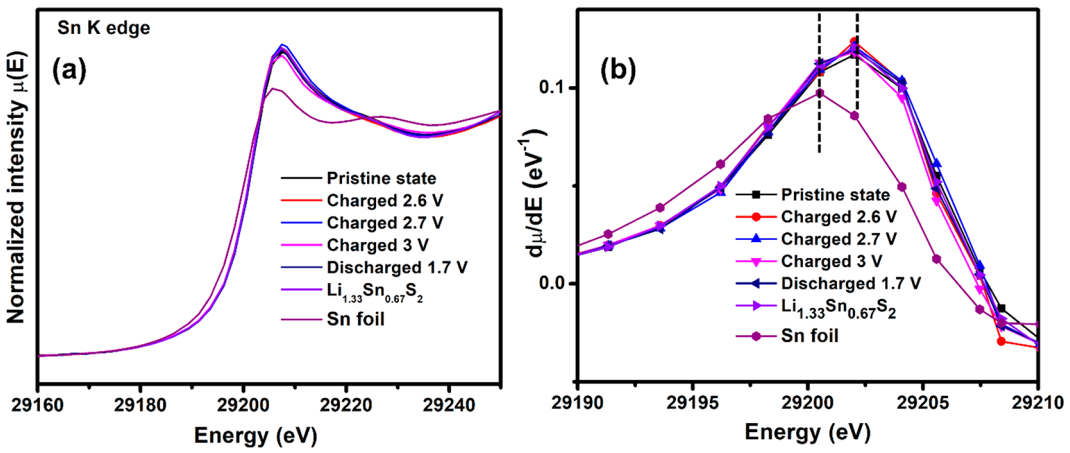

Figure 5. Ex situ hard X-ray XANES measurements of 0.2 Fe substituted active cathode compound at different states of charge. (a) Sn K edge XANES measurements of active electrode cycled at different states of charge. (b) First derivative of rising edge Sn K edge region of active material cycled at different states of charge.

state of charge of 3 V corresponding to the possible $Fe^{2+/3+}$ redox reaction. Upon discharged to 1.7 V, the Fe $L_{2,3}$ edge was further shifted back to lower energy, indicating the reversible Fe redox contribution to the observed electrochemical performance of the active material. However, the energy shifts were not completely recovered after discharge which may be attributed to the lithiation induced structural transformation which causes irreversibility with the redox reactions. Thus, the redox contribution of the cation Fe redox is identified through Fe L edge EELS measurements. From the electrochemical performance (Figure 1), a specific capacity value of ∼150 mAh/g at 10 mA/g was obtained without doing any nanosizing and engineering optimization. If we consider the $Fe^{2+/3+}$ redox, the maximum capacity out of the $Fe^{2+/3+}$ redox is ∼35 mAh/g capacity in the formula unit ($Li_{1.33-2y/3}Sn_{0.67-y/3}Fe_yS_2$, y = 0.2 gives $Li_{1.2}Sn_{0.6}Fe_{0.2}S_2$). Conventionally, the $Fe^{2+/3+}$ redox is quite prevalent in sulfide[43,44] and oxide structures,[45] and the high voltage $Fe^{3+/4+}$ redox is not so common in cathodes.[46] Thus, we believe that the capacity contribution obtained from this sulfide framework could be of exploiting the $Fe^{2+/3+}$ redox in the potential region of 1.7−3 V vs Li/Li^+. After confirming the Fe redox participation through metal L edge EELS measurements, the possible sulfur anion redox participation was investigated in the same set of samples. The S L-edge spectra with weak pre-edge and strong main edge peaks are shown in Figure 4b. The observed weak pre-edge and sharp rising edge peaks are attributed to the transition between the S 2p states to the unoccupied molecular orbital states.[47] The pre-edge feature is mainly dominated by the transition of electrons from S 2p to S 3s states, with hybridization character of metal 3d orbitals. Further, the sharp edge corresponds to the 2p core level transition to unoccupied molecular orbitals of S 3s, S 3d 4s, etc.[47] From the S L edge features, these spectra could be used to qualitatively understand the elemental redox participation in various composition ranges. After completely charged to 3 V, the main peaks rising edge was shifted to high energy, corresponding to the improved covalency between ligand p states and metal d states due to the partial oxidation of the sulfide anion.[48] This observation confirms the S ligand redox participation in this cathode material.

After identifying the Fe and S redox participation, another possible elemental activity of Sn was identified through synchrotron hard X-ray Sn K edge X-ray absorption spectroscopy (XAS) measurements (Figure 5). The Sn K edge measurements were collected in various state of charge samples including the pristine state, charged to 2.6, 2.7, 3.0 V, and discharged to 1.7 V. Figure 5a shows the Sn K edge X-ray absorption near-edge structure (XANES) spectra with different state of charge samples along with Sn metal reference foil and $Li_{1.33}Sn_{0.67}S_2$. The Sn K edge data were processed (normalization, calibration, and energy alignment) with the Athena software package.[49] All Sn K edge spectra were energy aligned with respect to the first derivative peak of the Sn reference foil at 29200.4 eV as described in Kraft et al.[50] In the Fe substituted composition, the Sn and Fe elements are present in tetravalent Sn^{4+} and divalent Fe $^{2+}$ valence states, respectively. The tetravalent Sn^{4+} state is a fully filled d^{10} orbital configuration that is not electrochemically active in the potential range of 1.7−3 V. Therefore, the Li extraction/insertion reaction is believed to be compensated by the $Fe^{2+/3+}$ redox and partial sulfur anion redox reaction which contributed toward the specific capacity of ∼150 mAh/g at 10 mA/g current density. This explanation was further evidenced with the Sn K edge XANES spectra that the edge energy of Fe subsituted cathodes did not show any shift of both high energy and low energy during different states of charge. Also, Sn K edge spectra of cathode compositions have higher edge energy than the Sn reference foil, corresponding to the high oxidation state of Sn^{4+} to Sn metal reference foil Sn^0. Apart from the energy shifts, the intensity of the near-edge region of the Sn K edge lowers when completely charged to 3 V, which may be attributed to the local bonding environmental changes at the different states of charge. To visualize the Sn K edge energy shift unambiguously, the first derivative of the rising edge of the Sn K edge region is shown in Figure 5b. As shown in Figure 5b, the rising edge energy shifts are negligible in the different state of charge materials, indicating that the Sn^{4+} is not contributed toward the Li insertion and extraction reactions. The Sn reference foil rising edge region in the first derivative spectrum has a significant energy difference which confirms the Sn elemental state in 0.2Fe-$Li_{1.33}Sn_{0.67}S_2$ is at its high oxidation state.

On the basis of the electrochemical activity of elements in the cathode, the rough estimation of the Fe and S contribution can be extracted from the observed electrochemical performance. When all the Li ions are extracted, the 0.2 Fe substitution

https://doi.org/10.1021/jacs.1c06828
J. Am. Chem. Soc. 2021, 143, 15732−15744

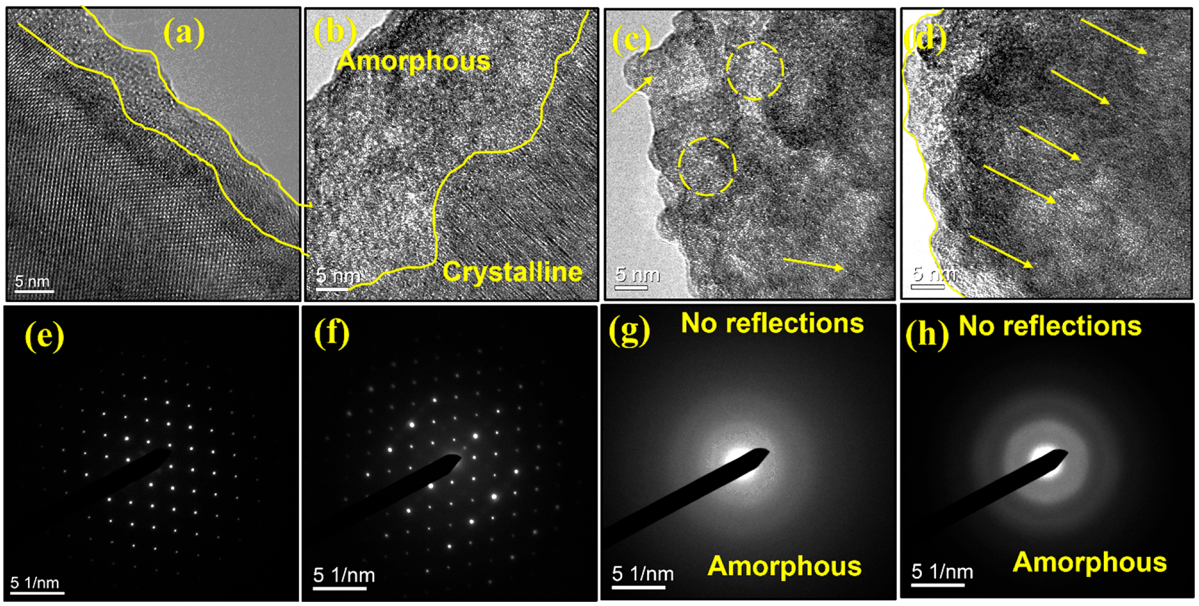

Figure 6. Structural evolution of active cathode cycled at different states of charge. HR-TEM and its associated SAED patterns of (a, e) pristine, (b, f) 2nd cycle discharged state, (c, g) 2nd discharged state of surface with the amorphous region, and (d, h) cycled electrode with complete amorphous region. (Yellow-colored circles and arrows indicate degraded spots and directions, respectively.)

(expected formula $Li_{1.2}Sn_{0.6}Fe_{0.2}S_2$) can deliver 208 mAh/g capacity (based on 1.2 Li) irrespective of irreversibility. However, the practical electrochemical capacity of 150 mAh/g (~0.9 Li) was observed without doing any nanosizing and engineering optimizations. Therefore, the observed capacity is compensated roughly by 0.2 $Fe^{2+/3+}$ of ~35 mAh/g and the remaining of ~115 mAh/g contributed by S anion redox. To further confirm the sulfur anion redox contribution, the XPS investigation was carried out on pristine and fully charged samples (Supporting Information, Figure S6). From the XPS spectra, the S^{2-} lattice sulfide peaks were deconvoluted into doublets in the range of 161−163 eV. The two peaks resulted from the spin-orbit doublet S $2p_{1/2}$ and S $2p_{3/2}$. At higher binding energy, a peak at ~163.6 eV is due to the possible sulfide redox state variation, and the same binding energy values were previously assigned to short-chain polysulfide species in sodium-based layered cathodes.[31,51] We assign the S_2^{n-} to the feature emerged in the fully charged state, and the feature was not observed in the same binding energy region at the pristine state which confirms the possible sulfur redox state variation at the high state of charge. The broad features at the high binding energy around 170 eV are associated with the surface oxygen traces of sulfites and sulfates. To further identify the S redox mechanism, the ex situ Raman spectroscopy was used and the Raman spectra for different states of charge samples are shown in Figure S7. The Raman spectra clearly exhibited an M-S vibration around the 300 cm^{-1} region and the possible dimer regions at the ~500 and ~650 cm^{-1}. The observed feature was similar to reported literature,[30,52] and further analysis is needed to clearly identify the dimer mechanism of this anion redox reaction. Despite the sulfide cathode chemistry exhibiting a low voltage plateau than oxides, sulfide candidates are excellent as they exhibit a sulfide anion redox potential lower than the stability window of the conventional organic electrolytes. Even after rigorous research in the field of anion redox chemistry, the Li-rich oxide cathodes have not been successful yet due to their unsolved fundamental issues of voltage fade, voltage hysteresis, and irreversible oxygen release, and the rational understanding of the failure mechanism is still not clear.[53] On the other hand, the Li-rich sulfide anion redox cathode chemistry is emerging and exhibited highly reversible anion redox chemistry due to improved metal−ligand covalency compared to highly argued oxygen anion redox cathode chemistry.[29] In addition, the anion and cation redox competition behavior in transition metal chalcogenides was understood by many researchers, especially a seminal work by Rouxel et al. in 1996.[27] With this fundamental advantage, this cathode chemistry could lead to the acceleration of the research direction to understand the mixed anionic and cationic redox chemistry in various metal ligand environments.

Triggering Sulfide Anion Redox Mechanism. In this work, substitution of the d orbital metal redox couple acts as a redox center and further triggered the anion redox in a sulfide framework. This triggering event in anion redox chemistry with a cation redox was achieved due to the "*redox couple pinning*" of $Fe^{2+/3+}$ on top of the sulfide framework ($Li_{1.33}Sn_{0.67}S_2$). This redox couple pinning mechanism allows the partially filled d states to move to the top of an anion p band when the d state changes to high oxidation. As introducing the redox couple on top of the anion p band, the redox couple d band penetrates the anion p band which leads to covalent mixing of the redox couple d-band and p-band orbitals. When the metal redox center is sufficiently oxidized, the orbital mixing event has an additional electron source from the anion (which is sulfide anion here) during Li-ion extraction.[53] With this fundamental theory, once the Fe^{2+} substituted in $Li_{1.33}Sn_{0.67}S_2$, the Fe redox couple is pinned well on top of the sulfide anion 3p band and facilitates the electron transfer reaction from the sulfide anion after Fe^{2+} oxidation. This $Fe^{2+/3+}$ redox couple pinning character is an added advantage to be used in assessing various 3d metal ligand-based sulfide anion redox cathode materials for Li-ion batteries. With this understanding, when the Fe substitution is relatively large, the Fe d state character will dominate near the Fermi level, and the improved d character may raise the Fermi level. Since the Fermi level has a

https://doi.org/10.1021/jacs.1c06828
J. Am. Chem. Soc. 2021, 143, 15732−15744

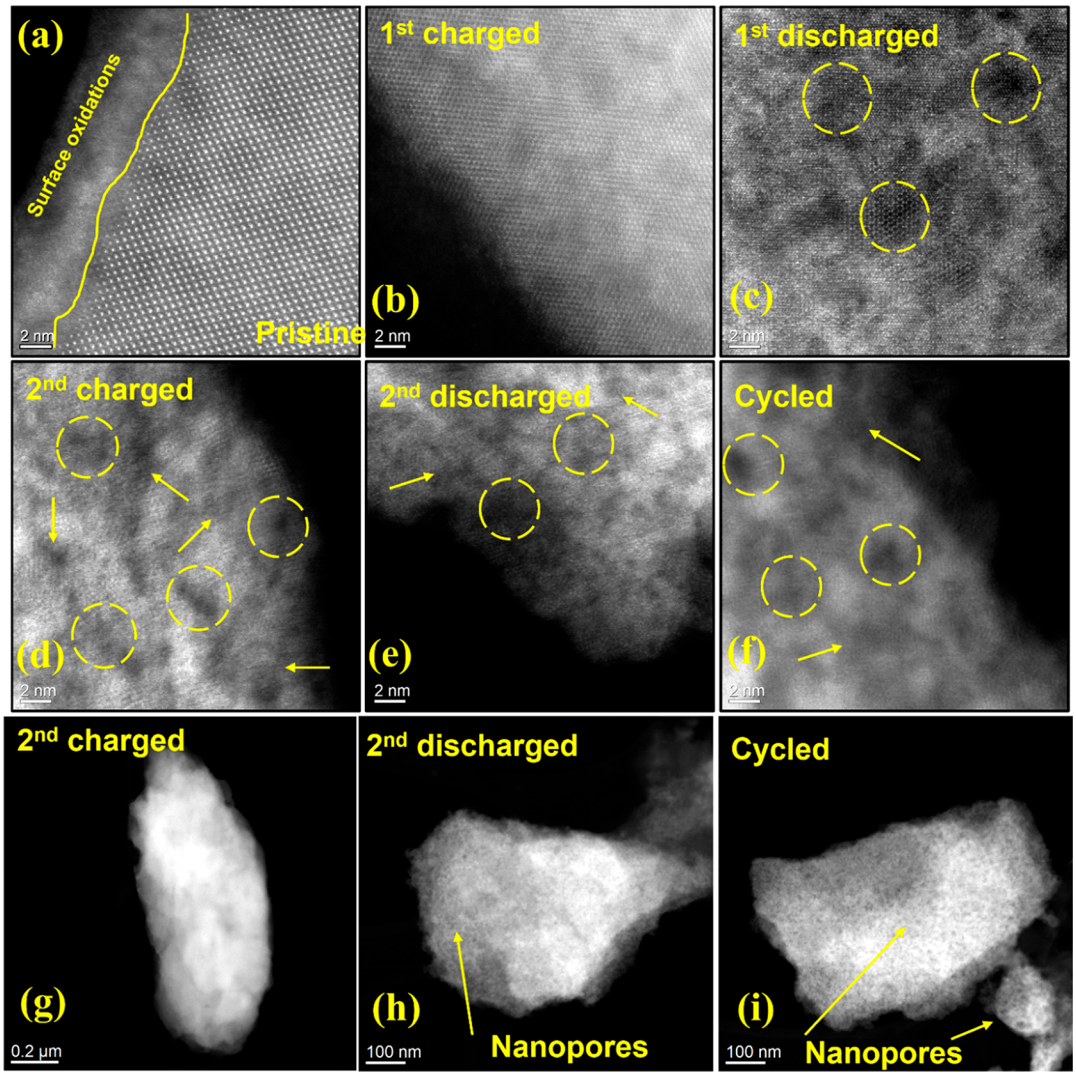

Figure 7. HAADF-STEM investigation of the 0.2Fe-$Li_{1.33}Sn_{0.67}S_2$composite electrode at different states of charge: (a) pristine, (b) 1st charged, (c) 1st discharged, (d, g) 2nd charged, (e, h) 2nd discharged, (f, i) cycled electrodes. The yellow-colored circles and arrow markings show clearly the nanoscale degraded regions of the cathode materials after different state of cycling conditions. In panel (c), the honeycomb ordering was visualized and marked as yellow circles. The yellow circles in the other figures exhibit the structural degradation induced as a result of extended cycling.

direct correlation to electrochemical potential, increasing Fe substitution will influence the electrochemical lithiation-delithiation potentials, and further, the improved d character will limit the anion redox reaction which is why the high Fe substitution exhibits less capacity than others (Figure 1d).

Possible Failure Mechanism through Microscopy Investigation. Though the Sn-based chalcogen cathode exhibited mixed cationic and anionic redox, voltage fade and gradual capacity fade issues are nested to the cathode material during electrochemical cycling. To date, the similar voltage and capacity fade mechanisms in Li- and Mn-rich oxide cathode materials were investigated with various spectroscopy and microscopy probes by numerous research groups.[14,54,55] Here, by examining morphological changes associated with electrochemical reactions of this cathode, it is possible to determine the mechanism of their degradation processes and origin of capacity fade mechanisms induced by electrochemical reactions. Therefore, to evaluate structural modifications of the active materials after electrochemical reactions, a detailed microscopy investigation was carried out using high-resolution transmission electron microscopy (HR-TEM) and high annular dark field-scanning transmission electron microscopy (HAADF-STEM) investigations. In this detailed microscopy investigation, the high-resolution HRTEM micrographs and their associated selected area electron diffraction (SAED) patterns are shown in Figure 6, while the Z-contrast HAADF-STEM images are shown in Figure 7. The samples of active cathode material at different cycled states were used for this microscopy investigation. Extreme care was taken to avoid possible air contamination by preparing the samples inside a glovebox and transferring them to the standard TEM sample holder inside the glovebox. The HR-TEM and SAED patterns of pristine, 2nd discharged, and cycled conditions are shown in Figure 6, while 1st charged, 1st discharged, and 2nd charged conditions are shown in the Supporting Information (Figure S8). From the HRTEM images, the pristine material before electrochemical reactions showed a crystalline ordered nature with lattice fringes of the layered structural framework (Figure 6a). The SAED pattern of this material further supported its crystalline nature with clear electron diffraction spots (Figure 6e). Because of surface oxidation, minimal surface layers are observed and highlighted in yellow markings. Further, the

https://doi.org/10.1021/jacs.1c06828
J. Am. Chem. Soc. 2021, 143, 15732−15744

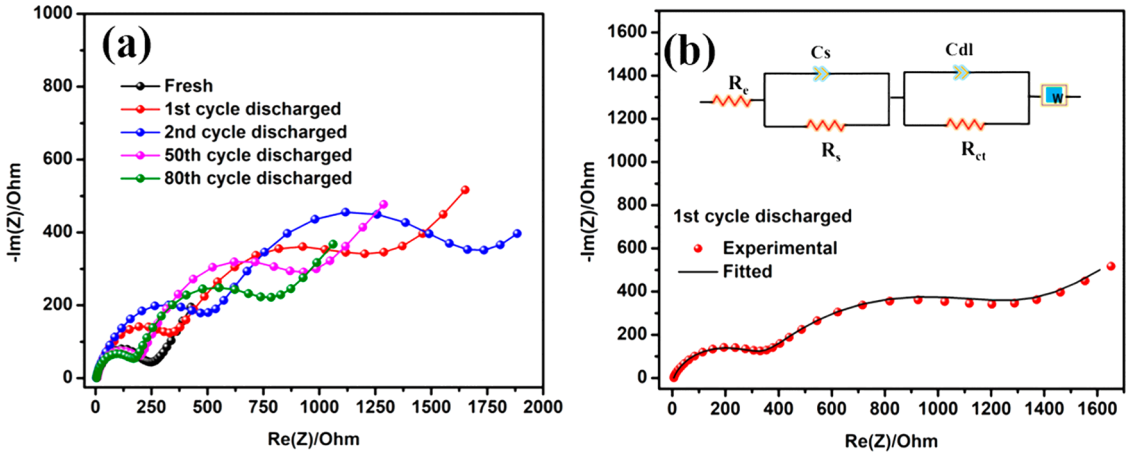

Figure 8. EIS investigation of 0.2Fe-$Li_{1.33}Sn_{0.67}S_2$ composite electrode cycled at different states of charge. (a) Nyquist plots of the composite electrode at different cycles; the EIS was recorded after the respective cycle was completed. (b) A typical EIS model was fitted to the experimental Nyquist plot.

cathode material after electrochemical reactions, especially 1st charged, discharged, and 2nd charged states, transformed to a disordered phase with crystalline domains. Interestingly, the degradation of the layered structural framework was clearly observed in the 2nd discharged state where the disordered amorphous region and ordered crystalline region are distinguished in the same particle (Figure 6b). This observation was supported with the SAED pattern which shows crystalline electron diffraction spots (Figure 6f). Further, the TEM micrograph of surface regions was imaged that showed clearly an amorphous region with no lattice fringes or ordered crystalline domains. To understand the extent of this amorphization, the cycled cathode material after 50 continuous charge-discharge cycles was investigated that exhibited complete amorphous regions, and the associated SAED patterns confirmed this observation by exhibiting an amorphous halo (Figure 6d,h). Also, the SAED pattern of the surface region also exhibited no electron diffraction spots due to amorphization during initial electrochemical reactions (Figure 6g). With these results, we confirm that the Li insertion-extraction reactions significantly transformed the crystal structure, and the active materials started losing crystallinity from the surface region during electrochemical reactions. This amorphization mechanism was triggered during initial Li insertion-extraction reactions and continued during extended cycling. Furthermore, this amorphization reaction mechanism could be the reason for constant capacity fade and voltage fade during cycling. We suspect that these significant degradation phenomena must be associated with loss in chemical constituents such as sulfur loss. Previously, the degradation due to sulfur loss was observed in chalcogen-based layered sulfide cathode material and correlated toward electrochemical reactions.[30] Therefore, to evidence this relation between amorphization and sulfur loss, we attempted S L edge measurements in the same set of samples (Figure S9). Surprisingly, after the initial cycle (1st cycle), the 2nd cycle and cycled samples exhibit less S L edge intensity compared to the pristine and 1st cycle, which confirms the loss in S during the electrochemical reactions. The normalization of S L edge spectra on a different set of samples was performed with reference to pristine S L edge spectra. In summary, the TEM investigation evidences that the Li insertion-extraction reactions significantly induced structural inhomogeneity starting from the surface of the cathode materials, resulting in highly localized amorphization due to sulfur loss-induced degradation. In comparison to oxide cathodes, severe degradation phenomena such as pore formation and crack formation were evidenced as a result of oxygen loss in various high voltage layered oxide cathodes previously.[14,56−58] Similarly, we expect that the observed sulfur loss phenomena also could be associated with morphology changes during cycling. In general, pore regions and crack formation could be clearly seen in dark field HAADF-STEM investigations because this Z-contrast imaging technique is highly sensitive to variations in the atomic number of atoms in the samples. In the pore and less dense regions, the average atomic number is low. Therefore, introducing this Z-contrast technique will clearly elucidate possible sulfur loss-induced degradations such as pore and crack formation at the active materials after cycling. The structural evolution due to Li insertion-extraction was visualized in a series of samples using HAADF-STEM images (Figure 7). The bright spots in the images represent high atomic number elements such as transition metals, and the light elements such as Li, S, and O will not show up as bright spots. From the detailed Z-contrast HAADF investigations in the cycled samples, the porosity formation and severe structural distortions were identified after cycling.

Figure 7a shows the ordered pristine cathode composition, which exhibits bright spots of metal elements, and the lattice exhibits no distortions or cracks regions. However, after the 1st cycle, the lattice showed severe structural distortions and nanopore formation that are identified as yellow-colored circles and arrows in the figure (Figure 7c−f). Interestingly, the structural distortion was well identified in the discharged state sample (1st discharged) in which the honeycomb ordering was observed and the ordered crystalline domain lost crystallinity after consequent cycling (Figure 7c). Upon further investigation, we found that the pores and structural distortions were extreme, and the crystalline domains were degraded, leading to a complete distorted structure after cycling. As evidenced in Figure 7a−f, the degradation mechanism (pore and crack formation) progressed from during initial cycles to extended cycling conditions. The cycled electrode exhibited severe degradation compared to initial cycles that is strongly supporting our HRTEM observation of amorphization. Further, to identity nanopore regions in a complete particle,

https://doi.org/10.1021/jacs.1c06828
J. Am. Chem. Soc. 2021, 143, 15732−15744

low magnification images of 2nd charged, 2nd discharged, and cycled samples are shown in Figure 7g,h where a lot of nanopores throughout the particle were identified in the cycled cathode. This once again confirms that the nanopore formation is due to the sulfur loss degradation process and was accelerated due to extended Li insertion-extraction reactions. To date, this nanopore/nanovoid formation due to oxygen loss in the Li-rich oxide anion redox cathode and their degradation mechanisms are investigated with correlation to fundamental issues of voltage fade, voltage hysteresis, and capacity fade mechanisms.[14,58] Since the sulfide anion is a significant charge contributor during Li extraction, the sulfur loss induced amorphization phenomenon is a nanoscale evolution and the loss in sulfur is directly reflected in charge-discharge voltage profiles and constant capacity fade of the cycled cathode materials. On the basis of the detailed experimental evidence, it is confirmed that the sulfur loss and amorphization reactions are coupled degradation mechanisms rather than separate degradation mechanisms.

After understanding structural and electrochemical investigations, to understand the resistance factors induced by the insertion-extraction reactions at the electrode-electrolyte interface, the EIS analysis was performed at the different cycled conditions. Figure 8a shows the Nyquist plots of active cathode material at different discharged cycles. The measurement was carried out in the coin cell with Li foil as reference and counter electrodes. The active materials coated on Al foil is used as the working electrode. In this two-electrode system, the EIS contribution is previously proved to be mainly from positive electrodes.[59] Therefore, we correlate the EIS results with a major focus of the positive electrode while neglecting minimal contribution from the Li metal foil counter electrode. All the EIS measurements exhibit two semi-circle regions except for the pristine cell. The high frequency semi-circle region corresponds to the surface film formation on the positive electrodes, and the second low frequency region corresponds to the charge transfer resistance upon Li^+ insertion-extraction. Furthermore, a sloppy line is called Warburg diffusion (W) in the electrolyte bulk. With this understanding, the EIS data were fitted with an equivalent circuit model (Figure 8b) and the resistance values for all the active materials at different cycles were tabulated in Table S1. From the model, the R_e corresponds to the solution resistance, and also, this is considered as uncompensated resistance in electrochemical cells. The R_s and C_s correspond to the surface film resistance and capacitance of the active sulfide composite cathode, respectively. Finally, the Li insertion and extraction induced charge transfer resistance and double layer capacitance will be accounted for R_{ct} and C_{dl} parameters, respectively. From the Figure 8a and Table S1, the R_e values for all the materials exhibited minimal difference for all the cycles, implying that the electrolyte is stable during electrochemical cycling. During 1st and 2nd cycles, the R_s and R_{ct} values increased proportionally to the initial cycle number, indicating that the structural distortion during initial cycles caused significant changes at the electrode and electrolyte interface. This observation was supported by GITT analysis (Figure 2) that the huge overpotential during lithium insertion (discharge) of initial cycles is due to the kinetic limitation of Li insertion reactions which was further reflected in the EIS measurements. In addition, the structural transformations during initial cycles were well evidenced with the microscopy investigation previously. Further, the R_s values of cycled electrodes exhibit negligible difference which is due to the stable film formation after the initial cycles. In general, most of the surface film formation will occur during initial cycling. However, the R_{ct} values decreased proportionally over extended cycling, exhibiting a trend that the resistance factors increased during initial cycles and decreased during extended cycling. This phenomenon may be due to the sulfur loss induced by extended cycling conditions in which the complete amorphization and nanopore formation were also observed through microscopy investigation. We assume that the anion redox induced sulfur loss may reduce the Li insertion-extraction abilities, thereby showing gradual capacity fade during cycling that could be correlated to the decrease in the charge transfer resistance in the EIS. These findings in the Sn-based chalcogen layered framework as a mixed redox cathode is new, and further studies will be carried out to explore this family of cathode chemistry for dual anionic and cationic redox cathode materials.

CONCLUSION

In summary, a new Sn-based chalcogen cathode was identified and its Li^+ insertion and extraction properties were understood to follow a dual anionic and cationic redox mechanism. The chalcogen anion redox was triggered by improving the metal−ligand covalency approach where the partially filled d orbital redox couple was introduced into the chalcogen-based Li_2SnS_3 structural framework. From the electrochemical investigation, this chalcogen-based structural framework reversibly exhibited Li^+ insertion and extraction properties even in the high loading conditions. The charge compensation was achieved by exploiting $Fe^{2+/3+}$ redox and S^{2-}/S_2^{n-} redox reactions. The layered crystalline phase was identified by substituting the $Fe^{2+/3+}$ redox couple in a Li-ion conducting phase $Li_{1.33}Sn_{0.67}S_2$ with different compositional regimes. Further, the EELS spectra were used to identify possible Fe and S redox contributions, and the electrochemical inactivity of Sn^{4+} in the active material composition was identified using XANES spectra. Furthermore, an in-depth HR-TEM and HAADF-STEM analysis revealed the severe surface amorphization and nanopore formations at the cathode particles due to sulfur loss associated with the mixed anionic and cationic redox reactions. This is the first time that the Sn-based chalcogen framework with an Fe redox couple crystalline phase was explored for potential application in Li-ion cathode materials. The experimental insights provide a significant design approach that will accelerate the search for prospective Ni and Co free chalcogen-based cathodes in the pursuit of next-generation energy storage materials.

ASSOCIATED CONTENT

Supporting Information

The Supporting Information is available free of charge at https://pubs.acs.org/doi/10.1021/jacs.1c06828.

Experimental and material characterization, photographs of synthesized materials, EDS maps of the 0.2 Fe substituted cathode, powder diffraction of all compounds, CV profiles of active cathode material, CD profiles of 0.1 Fe and 0.4 Fe substituted cathode materials, CD profiles of high loading cell, XPS and Raman analysis of active material, EELS investigation, EIS table (PDF)

https://doi.org/10.1021/jacs.1c06828
J. Am. Chem. Soc. 2021, 143, 15732−15744

AUTHOR INFORMATION

Corresponding Author

Leela Mohana Reddy Arava − *Department of Mechanical Engineering, Wayne State University, Detroit, Michigan 48202, United States;* orcid.org/0000-0001-6685-6061; Email: leela.arava@wayne.edu

Authors

Sudhan Nagarajan − *Department of Mechanical Engineering, Wayne State University, Detroit, Michigan 48202, United States*

Sooyeon Hwang − *Center for Functional Nanomaterials, Brookhaven National Laboratory, Upton, New York 11973, United States;* orcid.org/0000-0001-5606-6728

Mahalingam Balasubramanian − *X-ray Science Division, Advanced Photon Source, Argonne National Laboratory, Lemont, Illinois 60439, United States*

Naresh Kumar Thangavel − *Department of Mechanical Engineering, Wayne State University, Detroit, Michigan 48202, United States;* orcid.org/0000-0002-6604-0211

Complete contact information is available at: https://pubs.acs.org/10.1021/jacs.1c06828

Notes

The authors declare no competing financial interest.

ACKNOWLEDGMENTS

This material is based upon work supported by the National Science Foundation under Grant No. 2127519. This research used resources of the Center for Functional Nanomaterials, which is a U.S. DOE Office of Science Facility, at Brookhaven National Laboratory under Contract No. DE-SC0012704. This research used resources of the Advanced Photon Source, a U.S. Department of Energy (DOE) Office of Science User Facility, operated for the DOE Office of Science by Argonne National Laboratory under Contract No. DE-AC02-06CH11357. We acknowledge the Choudhury group, Missouri S&T for material synthesis, and the Lumigen Instrument Centre at Wayne State University for the use of XPS (NSF: MRI 1849578) and XRD (NSF: MRI 1427926) facility.

REFERENCES

(1) Whittingham, M. S. Lithium batteries and cathode materials. *Chem. Rev.* **2004**, *104* (10), 4271−4302.

(2) Goodenough, J. B.; Kim, Y. Challenges for Rechargeable Li Batteries. *Chem. Mater.* **2010**, *22* (3), 587−603.

(3) Assat, G.; Tarascon, J. M. Fundamental understanding and practical challenges of anionic redox activity in Li-ion batteries. *Nature Energy* **2018**, *3* (5), 373−386.

(4) Croy, J. R.; Balasubramanian, M.; Gallagher, K. G.; Burrell, A. K. Review of the US Department of Energy's "Deep Dive" effort to understand voltage fade in Li-and Mn-rich cathodes. *Acc. Chem. Res.* **2015**, *48* (11), 2813−2821.

(5) Pang, W. K.; Alam, M.; Peterson, V. K.; Sharma, N. Structural evolution of electrodes in the NCR and CGR cathode-containing commercial lithium-ion batteries cycled between 3.0 and 4.5 V: An operando neutron powder-diffraction study. *J. Mater. Res.* **2015**, *30* (3), 373−380.

(6) Clément, R. J.; Lun, Z.; Ceder, G. Cation-disordered rocksalt transition metal oxides and oxyfluorides for high energy lithium-ion cathodes. *Energy Environ. Sci.* **2020**, *13* (2), 345−373.

(7) Sathiya, M.; Rousse, G.; Ramesha, K.; Laisa, C. P.; Vezin, H.; Sougrati, M. T.; Doublet, M. L.; Foix, D.; Gonbeau, D.; Walker, W.; Prakash, A. S.; Ben Hassine, M.; Dupont, L.; Tarascon, J. M. Reversible anionic redox chemistry in high-capacity layered-oxide electrodes. *Nat. Mater.* **2013**, *12* (9), 827−835.

(8) Sathiya, M.; Abakumov, A. M.; Foix, D.; Rousse, G.; Ramesha, K.; Saubanère, M.; Doublet, M. L.; Vezin, H.; Laisa, C. P.; Prakash, A. S.; Gonbeau, D.; VanTendeloo, G.; Tarascon, J. M. Origin of voltage decay in high-capacity layered oxide electrodes. *Nat. Mater.* **2015**, *14* (2), 230−238.

(9) McCalla, E.; Sougrati, M. T.; Rousse, G.; Berg, E. J.; Abakumov, A.; Recham, N.; Ramesha, K.; Sathiya, M.; Dominko, R.; Van Tendeloo, G.; Novák, P.; Tarascon, J.-M. Understanding the Roles of Anionic Redox and Oxygen Release during Electrochemical Cycling of Lithium-Rich Layered Li4FeSbO6. *J. Am. Chem. Soc.* **2015**, *137* (14), 4804−4814.

(10) Assat, G.; Foix, D.; Delacourt, C.; Iadecola, A.; Dedryvère, R.; Tarascon, J.-M. Fundamental interplay between anionic/cationic redox governing the kinetics and thermodynamics of lithium-rich cathodes. *Nat. Commun.* **2017**, *8* (1), 2219.

(11) Croy, J. R.; Garcia, J. C.; Iddir, H.; Trask, S. E.; Balasubramanian, M. Harbinger of hysteresis in lithium-rich oxides: Anionic activity or defect chemistry of cation migration. *J. Power Sources* **2020**, *471*, 228335.

(12) Lee, J.; Kitchaev, D. A.; Kwon, D.-H.; Lee, C.-W.; Papp, J. K.; Liu, Y.-S.; Lun, Z.; Clément, R. J.; Shi, T.; McCloskey, B. D.; Guo, J.; Balasubramanian, M.; Ceder, G. Reversible Mn2+/Mn4+ double redox in lithium-excess cathode materials. *Nature* **2018**, *556* (7700), 185−190.

(13) Eum, D.; Kim, B.; Kim, S. J.; Park, H.; Wu, J.; Cho, S.-P.; Yoon, G.; Lee, M. H.; Jung, S.-K.; Yang, W.; Seong, W. M.; Ku, K.; Tamwattana, O.; Park, S. K.; Hwang, I.; Kang, K. Voltage decay and redox asymmetry mitigation by reversible cation migration in lithium-rich layered oxide electrodes. *Nat. Mater.* **2020**, *19* (4), 419−427.

(14) Hu, E.; Yu, X.; Lin, R.; Bi, X.; Lu, J.; Bak, S.; Nam, K.-W.; Xin, H. L.; Jaye, C.; Fischer, D. A.; et al. Evolution of redox couples in Li- and Mn-rich cathode materials and mitigation of voltage fade by reducing oxygen release. *Nature Energy* **2018**, *3* (8), 690−698.

(15) Yamamoto, K.; Zhou, Y.; Yabuuchi, N.; Nakanishi, K.; Yoshinari, T.; Kobayashi, T.; Kobayashi, Y.; Yamamoto, R.; Watanabe, A.; Orikasa, Y.; Tsuruta, K.; Park, J.; Byon, H. R.; Tamenori, Y.; Ohta, T.; Uchimoto, Y. Charge Compensation Mechanism of Lithium-Excess Metal Oxides with Different Covalent and Ionic Characters Revealed by Operando Soft and Hard X-ray Absorption Spectroscopy. *Chem. Mater.* **2020**, *32* (1), 139−147.

(16) Naylor, A. J.; Makkos, E.; Maibach, J.; Guerrini, N.; Sobkowiak, A.; Björklund, E.; Lozano, J. G.; Menon, A. S.; Younesi, R.; Roberts, M. R.; Edström, K.; Islam, M. S.; Bruce, P. G. Depth-dependent oxygen redox activity in lithium-rich layered oxide cathodes. *J. Mater. Chem. A* **2019**, *7* (44), 25355−25368.

(17) Dai, K.; Wu, J.; Zhuo, Z.; Li, Q.; Sallis, S.; Mao, J.; Ai, G.; Sun, C.; Li, Z.; Gent, W. E.; Chueh, W. C.; Chuang, Y.-d.; Zeng, R.; Shen, Z.-x.; Pan, F.; Yan, S.; Piper, L. F. J.; Hussain, Z.; Liu, G.; Yang, W. High Reversibility of Lattice Oxygen Redox Quantified by Direct Bulk Probes of Both Anionic and Cationic Redox Reactions. *Joule* **2019**, *3* (2), 518−541.

(18) Yang, W.; Devereaux, T. P. Anionic and cationic redox and interfaces in batteries: Advances from soft X-ray absorption spectroscopy to resonant inelastic scattering. *J. Power Sources* **2018**, *389*, 188−197.

(19) House, R. A.; Rees, G. J.; Pérez-Osorio, M. A.; Marie, J.-J.; Boivin, E.; Robertson, A. W.; Nag, A.; Garcia-Fernandez, M.; Zhou, K.-J.; Bruce, P. G. First-cycle voltage hysteresis in Li-rich 3d cathodes associated with molecular O2 trapped in the bulk. *Nature Energy* **2020**, *5* (10), 777−785.

(20) Dogan, F.; Long, B. R.; Croy, J. R.; Gallagher, K. G.; Iddir, H.; Russell, J. T.; Balasubramanian, M.; Key, B. Re-entrant Lithium Local Environments and Defect Driven Electrochemistry of Li- and Mn-Rich Li-Ion Battery Cathodes. *J. Am. Chem. Soc.* **2015**, *137* (6), 2328−2335.

(21) Li, X.; Qiao, Y.; Guo, S.; Xu, Z.; Zhu, H.; Zhang, X.; Yuan, Y.; He, P.; Ishida, M.; Zhou, H. Direct Visualization of the Reversible

O2−/O− Redox Process in Li-Rich Cathode Materials. *Adv. Mater.* **2018**, *30* (14), 1705197.
(22) Hy, S.; Felix, F.; Rick, J.; Su, W. N.; Hwang, B. J. Direct in situ observation of Li2O evolution on Li-rich high-capacity cathode material, $Li[Ni_xLi_{(1-2x)/3}Mn_{(2-x)/3}]O_2$ $(0 \leq x \leq 0.5)$. *J. Am. Chem. Soc.* **2014**, *136* (3), 999−1007.
(23) Pearce, P. E.; Perez, A. J.; Rousse, G.; Saubanère, M.; Batuk, D.; Foix, D.; McCalla, E.; Abakumov, A. M.; Van Tendeloo, G.; Doublet, M.-L.; Tarascon, J.-M. Evidence for anionic redox activity in a tridimensional-ordered Li-rich positive electrode *β*-Li2IrO3. *Nat. Mater.* **2017**, *16* (5), 580−586.
(24) Li, H.; Perez, A. J.; Taudul, B.; Boyko, T. D.; Freeland, J. W.; Doublet, M.-L.; Tarascon, J.-M.; Cabana, J. Elucidation of Active Oxygen Sites upon Delithiation of Li3IrO4. *ACS Energy Letters* **2021**, *6* (1), 140−147.
(25) Blandeau, L.; Ouvrard, G.; Calage, Y.; Brec, R.; Rouxel, J. Transition-metal dichalcogenides from disintercalation processes. Crystal structure determination and Mossbauer study of Li2FeS2 and its disintercalates LixFeS2 (0.2⩽ x⩽ 2). *J. Phys. C: Solid State Phys.* **1987**, *20* (27), 4271.
(26) Rouxel, J. Some solid state chemistry with holes: Anion−cation redox competition in solids. *Curr. Sci.* **1997**, *73* (1), 31−39.
(27) Rouxel, J. Anion−Cation Redox Competition and the Formation of New Compounds in Highly Covalent Systems. *Chem.—Eur. J.* **1996**, *2* (9), 1053−1059.
(28) Saha, S.; Assat, G.; Sougrati, M. T.; Foix, D.; Li, H.; Vergnet, J.; Turi, S.; Ha, Y.; Yang, W.; Cabana, J.; Rousse, G.; Abakumov, A. M.; Tarascon, J.-M. Exploring the bottlenecks of anionic redox in Li-rich layered sulfides. *Nature Energy* **2019**, *4* (11), 977−987.
(29) Hansen, C. J.; Zak, J. J.; Martinolich, A. J.; Ko, J. S.; Bashian, N. H.; Kaboudvand, F.; Van der Ven, A.; Melot, B. C.; Nelson Weker, J.; See, K. A. Multielectron, Cation and Anion Redox in Lithium-Rich Iron Sulfide Cathodes. *J. Am. Chem. Soc.* **2020**, *142* (14), 6737−6749.
(30) Wang, T.; Ren, G.-X.; Shadike, Z.; Yue, J.-L.; Cao, M.-H.; Zhang, J.-N.; Chen, M.-W.; Yang, X.-Q.; Bak, S.-M.; Northrup, P.; Liu, P.; Liu, X.-S.; Fu, Z.-W. Anionic redox reaction in layered NaCr2/3Ti1/3S2 through electron holes formation and dimerization of S−S. *Nat. Commun.* **2019**, *10* (1), 4458.
(31) Flamary-Mespoulie, F.; Boulineau, A.; Martinez, H.; Suchomel, M. R.; Delmas, C.; Pecquenard, B.; Le Cras, F. Lithium-rich layered titanium sulfides: Cobalt- and Nickel-free high capacity cathode materials for lithium-ion batteries. *Energy Storage Materials* **2020**, *26*, 213−222.
(32) Brant, J. A.; Massi, D. M.; Holzwarth, N.; MacNeil, J. H.; Douvalis, A. P.; Bakas, T.; Martin, S. W.; Gross, M. D.; Aitken, J. A. Fast lithium ion conduction in Li2SnS3: synthesis, physicochemical characterization, and electronic structure. *Chem. Mater.* **2015**, *27* (1), 189−196.
(33) Zhang, W.; Seo, D.-H.; Chen, T.; Wu, L.; Topsakal, M.; Zhu, Y.; Lu, D.; Ceder, G.; Wang, F. Kinetic pathways of ionic transport in fast-charging lithium titanate. *Science* **2020**, *367* (6481), 1030−1034.
(34) Islam, M. S.; Driscoll, D. J.; Fisher, C. A. J.; Slater, P. R. Atomic-Scale Investigation of Defects, Dopants, and Lithium Transport in the LiFePO4 Olivine-Type Battery Material. *Chem. Mater.* **2005**, *17* (20), 5085−5092.
(35) Brec, R.; Prouzet, E.; Ouvrard, G. Redox processes in the LixFeS2/Li electrochemical system studied through crystal, Mössbauer, and EXAFS analyses. *J. Power Sources* **1989**, *26* (3), 325−332.
(36) Goodenough, J. B.; Kim, Y. Locating redox couples in the layered sulfides with application to Cu [Cr2] S4. *J. Solid State Chem.* **2009**, *182* (10), 2904−2911.
(37) Jacquet, Q.; Iadecola, A.; Saubanère, M.; Li, H.; Berg, E. J.; Rousse, G.; Cabana, J.; Doublet, M.-L.; Tarascon, J.-M. Charge Transfer Band Gap as an Indicator of Hysteresis in Li-Disordered Rock Salt Cathodes for Li-Ion Batteries. *J. Am. Chem. Soc.* **2019**, *141* (29), 11452−11464.
(38) Yu, H.; Wang, Y.; Asakura, D.; Hosono, E.; Zhang, T.; Zhou, H. Electrochemical kinetics of the 0.5Li2MnO3·0.5LiMn0.42Ni0.42-Co0.16O2 'composite' layered cathode material for lithium-ion batteries. *RSC Adv.* **2012**, *2* (23), 8797−8807.
(39) Martinolich, A. J.; Zak, J. J.; Agyeman-Budu, D. N.; Kim, S. S.; Bashian, N. H.; Irshad, A.; Narayan, S. R.; Melot, B. C.; Nelson Weker, J.; See, K. A. Controlling Covalency and Anion Redox Potentials through Anion Substitution in Li-Rich Chalcogenides. *Chem. Mater.* **2021**, *33* (1), 378−391.
(40) Ramakrishnan, S.; Park, B.; Wu, J.; Yang, W.; McCloskey, B. D. Extended Interfacial Stability through Simple Acid Rinsing in a Li-Rich Oxide Cathode Material. *J. Am. Chem. Soc.* **2020**, *142* (18), 8522−8531.
(41) Zhu, Z.; Yu, D.; Yang, Y.; Su, C.; Huang, Y.; Dong, Y.; Waluyo, I.; Wang, B.; Hunt, A.; Yao, X.; et al. Gradient Li-rich oxide cathode particles immunized against oxygen release by a molten salt treatment. *Nature Energy* **2019**, *4* (12), 1049−1058.
(42) Tan, H.; Verbeeck, J.; Abakumov, A.; Van Tendeloo, G. Oxidation state and chemical shift investigation in transition metal oxides by EELS. *Ultramicroscopy* **2012**, *116*, 24−33.
(43) Dugast, A.; Brec, R.; Ouvrard, G.; Rouxel, J. Li2FeS2, a cathodic material for lithium secondary battery. *Solid State Ionics* **1981**, *5*, 375−378.
(44) Takada, K.; Michiue, Y.; Inada, T.; Kajiyama, A.; Kouguchi, M.; Kondo, S.; Watanabe, M.; Tabuchi, M. Lithium iron thio-phosphate: a new 3 V sulfide cathode. *Solid State Ionics* **2003**, *159* (3−4), 257−263.
(45) Sun, C.; Rajasekhara, S.; Goodenough, J. B.; Zhou, F. Monodisperse porous LiFePO4 microspheres for a high power Li-ion battery cathode. *J. Am. Chem. Soc.* **2011**, *133* (7), 2132−2135.
(46) Susanto, D.; Cho, M. K.; Ali, G.; Kim, J.-Y.; Chang, H. J.; Kim, H.-S.; Nam, K.-W.; Chung, K. Y. Anionic Redox Activity as a Key Factor in the Performance Degradation of NaFeO2 Cathodes for Sodium Ion Batteries. *Chem. Mater.* **2019**, *31* (10), 3644−3651.
(47) Farrell, S. P.; Fleet, M. E.; Stekhin, I. E.; Kravtsova, A.; Soldatov, A. V.; Liu, X. Evolution of local electronic structure in alabandite and niningerite solid solutions [(Mn,Fe)S, (Mg,Mn)S, (Mg,Fe)S] using sulfur K- and L-edge XANES spectroscopy. *Am. Mineral.* **2002**, *87* (10), 1321−1332.
(48) Li, D.; Bancroft, G.; Kasrai, M.; Fleet, M.; Feng, X.; Tan, K. S K- and L-edge X-ray absorption spectroscopy of metal sulfides and sulfates; applications in mineralogy and geochemistry. *Can. Mineral.* **1995**, *33*, 949−960.
(49) Ravel, B.; Newville, M. ATHENA, ARTEMIS, HEPHAESTUS: data analysis for X-ray absorption spectroscopy using IFEFFIT. *J. Synchrotron Radiat.* **2005**, *12* (4), 537−541.
(50) Kraft, S.; Stümpel, J.; Becker, P.; Kuetgens, U. High resolution x-ray absorption spectroscopy with absolute energy calibration for the determination of absorption edge energies. *Rev. Sci. Instrum.* **1996**, *67* (3), 681−687.
(51) Shadike, Z.; Zhou, Y.-N.; Chen, L.-L.; Wu, Q.; Yue, J.-L.; Zhang, N.; Yang, X.-Q.; Gu, L.; Liu, X.-S.; Shi, S.-Q.; Fu, Z.-W. Antisite occupation induced single anionic redox chemistry and structural stabilization of layered sodium chromium sulfide. *Nat. Commun.* **2017**, *8* (1), 566.
(52) Doan-Nguyen, V. V. T.; Subrahmanyam, K. S.; Butala, M. M.; Gerbec, J. A.; Islam, S. M.; Kanipe, K. N.; Wilson, C. E.; Balasubramanian, M.; Wiaderek, K. M.; Borkiewicz, O. J.; Chapman, K. W.; Chupas, P. J.; Moskovits, M.; Dunn, B. S.; Kanatzidis, M. G.; Seshadri, R. Molybdenum Polysulfide Chalcogels as High-Capacity, Anion-Redox-Driven Electrode Materials for Li-Ion Batteries. *Chem. Mater.* **2016**, *28* (22), 8357−8365.
(53) Assat, G.; Tarascon, J.-M. Fundamental understanding and practical challenges of anionic redox activity in Li-ion batteries. *Nature Energy* **2018**, *3* (5), 373−386.
(54) Lin, R.; Hu, E.; Liu, M.; Wang, Y.; Cheng, H.; Wu, J.; Zheng, J.-C.; Wu, Q.; Bak, S.; Tong, X.; Zhang, R.; Yang, W.; Persson, K. A.; Yu, X.; Yang, X.-Q.; Xin, H. L. Anomalous metal segregation in lithium-rich material provides design rules for stable cathode in lithium-ion battery. *Nat. Commun.* **2019**, *10* (1), 1650.
(55) Eum, D.; Kim, B.; Kim, S. J.; Park, H.; Wu, J.; Cho, S.-P.; Yoon, G.; Lee, M. H.; Jung, S.-K.; Yang, W.; Seong, W. M.; Ku, K.;

https://doi.org/10.1021/jacs.1c06828
J. Am. Chem. Soc. 2021, 143, 15732−15744

Tamwattana, O.; Park, S. K.; Hwang, I.; Kang, K. Voltage decay and redox asymmetry mitigation by reversible cation migration in lithium-rich layered oxide electrodes. *Nat. Mater.* **2020**, *19*, 419−427.
(56) Gu, M.; Belharouak, I.; Zheng, J.; Wu, H.; Xiao, J.; Genc, A.; Amine, K.; Thevuthasan, S.; Baer, D. R.; Zhang, J.-G.; et al. Formation of the spinel phase in the layered composite cathode used in Li-ion batteries. *ACS Nano* **2013**, *7* (1), 760−767.
(57) Ahmed, S.; Pokle, A.; Schweidler, S.; Beyer, A.; Bianchini, M.; Walther, F.; Mazilkin, A.; Hartmann, P.; Brezesinski, T.; Janek, J.; Volz, K. The Role of Intragranular Nanopores in Capacity Fade of Nickel-Rich Layered $Li(Ni_{1-x-y}Co_xMn_y)O_2$ Cathode Materials. *ACS Nano* **2019**, *13* (9), 10694−10704.
(58) Yan, P.; Zheng, J.; Tang, Z.-K.; Devaraj, A.; Chen, G.; Amine, K.; Zhang, J.-G.; Liu, L.-M.; Wang, C. Injection of oxygen vacancies in the bulk lattice of layered cathodes. *Nat. Nanotechnol.* **2019**, *14* (6), 602−608.
(59) Song, J. Y.; Lee, H. H.; Wang, Y. Y.; Wan, C. C. Two- and three-electrode impedance spectroscopy of lithium-ion batteries. *J. Power Sources* **2002**, *111* (2), 255−267.

https://doi.org/10.1021/jacs.1c06828
J. Am. Chem. Soc. 2021, 143, 15732−15744